Proceeding of the IEEE
International Conference on Robotics and Biomimetics
Dali, China, December 2019

Design and Analysis of a Variable-span and Cambered Span Morphing Wing for UAV

Guang Yang, Hongwei Guo and Rongqiang Liu
State Key Laboratory of Robotics and System
Harbin Institute of Technology
Harbin, Heilongjiang Province, China
18B908112@stu.hit.edu.cn

***Abstract* - The variable-span and cambered span morphing wing for unmanned aerial vehicle (UAV) can greatly improve its flight efficiency. In this work, a new extendable and bendable morphing wing with double driving is designed. The morphing skeleton of wing is composed of the basic unit module which is seven-bar mechanism in series. The rubber-filled corrugated sandwich corrugated skin is designed according to the requirement of morphing skeleton. The kinematics model of morphing skeleton that is composed of three modules in series is established, then the kinematics analysis of morphing skeleton is carried out, at last the expressions of the deformed position and driving angle are obtained. In the case of the same wing span, the influence of different rod length ratio on the maximum extension length of the morphing wing is analyzed, and the influence of different driving speed on the maximum bending angle under the same rod length ratio is compared and analyzed.**

Index Terms* - *Morphing wing; Variable-span; Cambered span.

I. INTRODUCTION

Unmanned aerial vehicle (UAV) will face different environments in flight. In order to achieve the best aerodynamic performance in different flight states, it is necessary to change the wing shape. The variable-span and cambered span morphing wing has become an important part in the design of morphing wing. The extendable and bendable morphing wing can significantly improve the flight efficiency and the maneuverability of UAV in flight [1-6].

It is more difficult to design morphing wing than fixed wing. The main difficulties are the design of morphing skeleton and morphing skin. Morphing skeleton needs to meet the requirements of deformation capacity, load-bearing capacity and low mass. Morphing skin needs to meet the requirements of smooth and continuous surface and bear the aerodynamic load before and after deformation.

In the field of variable-span morphing wing, several morphing skeletons have been designed and tested. Hao [7] had designed a variable-span morphing wing which is driven by air cylinder. Gao [8] designed a variable-span morphing wing based on articulated hinge structure. In the field of cambered span morphing wing, V. Sherrer [9] achieved wing bending by designing a combined truss wing mechanism to act as an elastic hinge. S. Lucato [10] designed a high authority shape morphing plate which is connected by a tetrahedral truss core and consists of a Kagome truss.

When the skeleton of wing is deformed, the skin on its surface also deforms. Morphing skin mainly takes two forms: elastic deformation of material itself and structural deformation of itself. The most representative elastic deformation of materials is rubber and shape memory polymer. The morphing skin of NextGen Aeronautics achieved large deformations by using silicone rubber as morphing skin [3]. Abrahamson uses shape memory composite material to design variable wing skin [11]. The most representative structural deformation based on itself is corrugated structure and honeycomb structure. Thill [12] and Yokozeki [13] designed a corrugated skin with rubber. Olympio [14] used honeycomb structure and flexible surface as morphing skin.

In order to achieve the simple structure, less drive and modularization of morphing wing, a new dual-drive morphing skeleton is proposed in this paper. The morphing skeleton is constructed by connecting together a repeating chain of "unit cell", forming a hybrid serial-parallel manipulator. The unit cell is seven-bar mechanism in the work. The rubber -filled corrugated sandwich corrugated skin is designed according to the requirement of morphing skeleton. The kinematics model of morphing skeleton that is composed of three modules in series is established, then complete the kinematics analysis of morphing skeleton, lastly discuss the effects of different rod lengths on the maximum extension length and the effects of different driving speed on the maximum bending angle.

II. DESIGN OF MORPHING WING

The main goal of this work is to design a new variable-span and cambered span morphing wing for UAV. Taking Rapture 40 UAV as an example, its original fixed wing structure is composed of rigid structures such as wooden wing ribs and wing beams. A low-speed airfoil with a good compromise between maximum lift coefficient and design simplicity is selected for the airfoil. Its structure is shown in Fig. 1 (a).

The main objective of this paper is to make the wing span of Rapture 40 UAV deformable and flexible in different flight missions, so that the lift-drag ratio of the wing can be improved by deforming in different flight states.

In the initial state, the wing span of UAV is in the minimum state of horizontal state. At this time, the minimum wing area can effectively reduce the space for UAV placement. When UAV takes off and landing, the lift-drag ratio and cruise time can be effectively improved by extending the wing span

978-1-7281-6321-5/19//$31.00 ©2019 IEEE

to the maximum and increasing the wing area. The wing extension structure of UAV is shown in Fig. 1 (b).

The main goal of this work is to design a new variable-span and cambered-span morphing wing for UAV. In this work, Rapture 40 UAV is used as a reference model to design the morphing wing. The initial state of UAV is in the minimum state of horizontal wing span, the minimum span can effectively reduce the UAV's resettlement space, as shown in Fig. 1 (a). When UAV takes off and landing, the lift-drag ratio can be effectively improved by extending the wing span, as shown in Fig. 1 (b). When UAV cruises, its wings need to bend upwards, which reduces its maneuverability and improves its stability, as shown in Fig. 1 (c). When UAV cruises, its wings need to bend upwards, which reduces its maneuverability and improves its stability, as shown in Fig. 1 (c). When UAV Pre-maneuvers, its wings need to bend downwards, which increases its maneuverability, as shown in Fig. 1 (d).

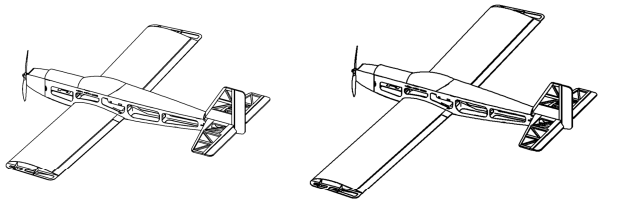

(a) Undeformed state of UAV (b) Span increment of morphing wing

(c) Wingspan upward bending of morphing wing (d) Wingspan downward bending of morphing wing.

Fig. 1 The UAV model with morphing wing.

Based on fixed wing of Rapture 40 UAV, this paper proposes a new dual-drive morphing wing that meet the requirements of UAV's flexibility, flexure and load. The morphing skeleton of wing is constructed by connecting together a repeating chain of “unit cell”, forming a hybrid serial-parallel manipulator, as shown in Fig. 2 (a). The rubber-filled corrugated sandwich corrugated skin of wing is designed according to the requirement of morphing skeleton, as shown in Fig. 2 (b).

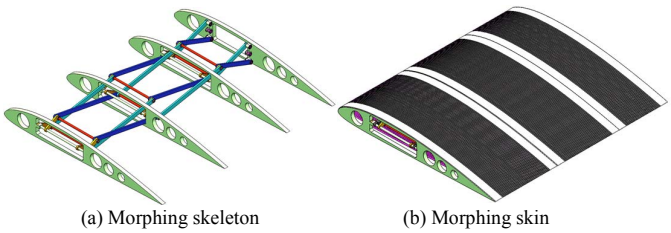

(a) Morphing skeleton (b) Morphing skin

Fig. 2 The variable-span and cambered-span morphing wing.

A. *Morphing Skin*

For UAVs, skin of wing is the main component bearing aerodynamic load, so the aerodynamic surface of skin before and after deformation should always be smooth, continuous and seamless. In order to achieve smooth, continuous and seamless skin deformation, it is necessary that the skin can produce a large amount of deformation to ensure the deformation characteristics, and enough stiffness is needed to maintain the aerodynamic shape of the wing during the deformation process, while reducing the loss of driver performance.

According to the deformation requirement, the morphing skin is designed as rigid-flexible coupling skin. The rigid part of morphing skin is made of thin plate, which is riveted and fixed on the rib plate. The flexible part of morphing skin adopts the rubber -filled corrugated sandwich corrugated skin scheme, which is fixed on the rigid skin, as shown in Fig. 3.

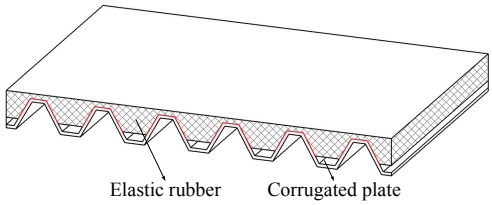

Fig. 3 The flexible part of morphing skin.

The rubber-filled corrugated sandwich corrugated skin is based on corrugated structure, and its surface is covered with elastic rubber with low modulus and high strain. It is bonded by heat-resistant glue. The elastic surface provides a smooth aerodynamic shape for the morphing skin, while the corrugated structure provides sufficient stiffness for the skin to bear aerodynamic loads. The rubber-filled corrugated sandwich corrugated skin has lower stretching and bending stiffness in the direction of corrugated expansion, and higher stiffness in other directions, so it has good bearing capacity.

B. *Morphing Skeleton*

In order to improve industrialization and scalability, the morphing skeleton is designed by modularization, which is composed of several meta-modules with the same structure in series, and the number of series is set by the structure. The wing root module is the driving unit, as shown in Fig. 4 (a), the other series modules are follower unit, as shown in Fig. 4 (b). The driving unit and follower unit are both seven-bar mechanisms, which has two symmetrical parallel RRR groups of links and one RP group connects two adjacent ribs.

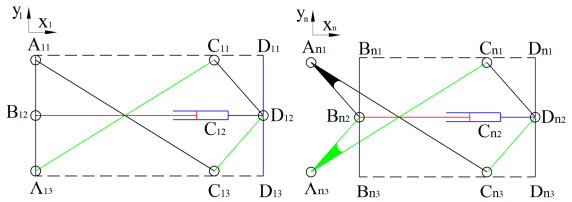

(a) Drive unit (b) Follower unit

Fig. 4 Component unit of morphing wing.

Fig. 4 (a) shows the configuration of the driving unit, it is a symmetrical structure which is represented by the fixed rib plate $A_{11}B_{12}A_{13}$, the moving rib plate $C_{12}D_{11}D_{12}D_{13}$, two driving links $A_{11}C_{13}$ and $A_{13}C_{11}$ and three passive links $C_{11}D_{12}$, $C_{13}D_{12}$ and $B_{12}C_{12}$. Link $B_{12}C_{12}$ and movable rib $C_{12}D_{11}D_{12}D_{13}$ are connected by sliding joints, and the other are connected by rotating joints. The origin of coordinate system is B_{12}, the x axis is along the direction of $B_{12}D_{12}$, and the y axis is along the direction of $B_{12}A_{11}$.

Fig. 4 (b) shows the configuration of the follower unit, it is the same as that of the driving unit. The fixed-ribbed plate $B_{n1}B_{n2}B_{n3}$ and the moving-ribbed plate $D_{(n-1)1}D_{(n-1)2}D_{(n-1)3}$ is the same, in which n>1. The driving links $A_{n1}B_{n2}$ and $A_{n3}B_{n2}$ of this unit are the same with the passive links $C_{(n-1)1}D_{(n-1)2}$ and $C_{(n-1)3}D_{(n-1)2}$ of the former unit, in which n>1. Link Bn2Cn2 and movable rib $C_{n2}D_{n1}D_{n2}D_{n3}$ are connected by sliding joints, and the other are connected by rotating joints. The origin of coordinate system is B_{n2}, the x axis is along the direction of $B_{n2}D_{n2}$, and the y axis is along the direction of $B_{n2}B_{n1}$.

In this work, three morphing modules are connected in series as an example. The initial state of the morphing wing is the minimum state of wingspan. In order to ensure that the skin does not appear bulging, the driving joint A_{11} of the active unit needs to be driven counterclockwise and the rotational speed needs to be marked as w_{11}, and the driving joint A_{13} of the active unit needs to be driven clockwise and the rotational speed needs to be marked as w_{13}. Active unit drive has four different working modes according to different driving speeds.

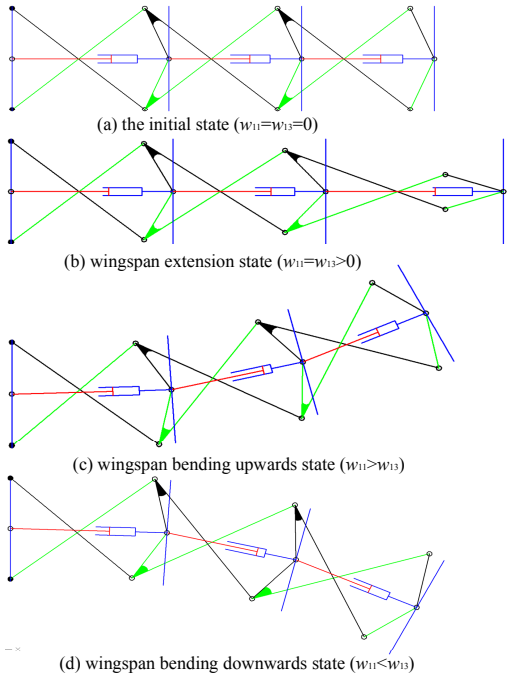

Fig. 5 Four working modes of the morphing skeleton.

The driving speed ratio of morphing wing is defined by parameters m ($m = w_{11}/w_{13}$). As shown in Fig. 5, named as (a) the initial state (w_{11}=w_{13}=0), (b) wingspan extension state (w_{11}=w_{13}>0), (c) wingspan bending upwards state (w_{11}>w_{13}), (d) wingspan bending downwards state (w_{11}<w_{13}).

III. Kinematic Analysis Of Morphing Skeleton

A. Kinematic Analysis of Driving Unit

In this step, it is assumed that all the geometrical dimensions of the mechanism are ideal. The geometric relations of links in the driving unit are shown in Fig. 6. The lengths of $A_{11}B_{12}$ and $B_{12}A_{13}$ are l_{01} and l_{02}, the lengths of $A_{11}C_{13}$ and $A_{13}C_{11}$ are l_{11} and l_{12}. The lengths of passive links $C_{11}D_{12}$, $C_{13}D_{12}$ and $B_{12}D_{12}$ are l_{13}, l_{14} and l_{15}, respectively. The angles between l_{11}, l_{12} and fixed rib plate $A_{11}B_{12}A_{13}$ respectively are θ_{11} and θ_{12} . The angles between l_{13}, l_{14} and dynamic rib plate $D_{11}D_{12}D_{13}$ respectively are θ_{13} and θ_{14} . The angles between l_{15} and current coordinate system x axis are θ_{15} .

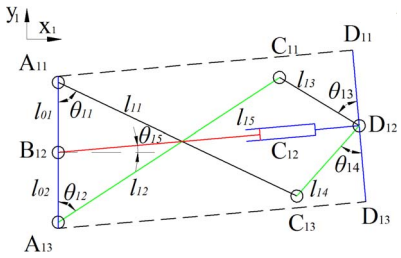

Fig. 6 Kinematic model of driving unit.

The origin of the global coordinate system is B_{12}, the X axis is along the direction of $B_{12}D_{12}$, and the Y axis is along the direction of $B_{12}A_{11}$. Position of the moving-ribbed plate in driving unit can be described by two coordinates:

$$\mathbf{q_1} = [x_{D12}, y_{D12}]^{\mathrm{T}} \tag{1}$$

Where x_{D12} and y_{D12} are the positions of the moving-ribbed plate in the driving unit coordinate system, θ_{15} is the angle between the fixed-ribbed plate and the moving-ribbed plate. For the driving unit, there exist the following constraint equations:

$$\mathbf{\Phi(q_1)} = \begin{bmatrix} l_{11}\sin\theta_{11} + l_{14}\sin(\theta_{14}-\theta_{15}) - x_{D12} \\ l_{12}\sin\theta_{12} + l_{13}\sin(\theta_{13}+\theta_{15}) - x_{D12} \\ l_{15}\cos\theta_{15} - x_{D12} \\ -l_{11}\cos\theta_{11} + l_{01} + l_{14}\cos(\theta_{14}-\theta_{15}) - y_{D12} \\ l_{12}\cos\theta_{12} - l_{02} - l_{13}\cos(\theta_{13}+\theta_{15}) - y_{D12} \\ l_{15}\sin\theta_{15} - y_{D12} \end{bmatrix} = \mathbf{0} \tag{2}$$

From (2), there is:

$$l_{14}^2 = (-l_{11}\sin\theta_{11} + x_{D12})^2 + (l_{11}\cos\theta_{11} - l_{01} + y_{D12})^2 \tag{3}$$

$$l_{13}^2 = (-l_{12}\sin\theta_{12} + x_{D12})^2 + (l_{12}\cos\theta_{12} - l_{02} - y_{D12})^2 \tag{4}$$

In the kinematic analysis, the inputs and outputs are concerned (3) and (4) can be rewritten as:

$$x_{D12} = k_1 + \frac{-k_2k_3 + k_2\sqrt{k_3^2 - k_4(1+k_2^2)}}{1+k_2^2} \tag{5}$$

$$y_{D12}=\frac{-k_3+\sqrt{k_3^2-k_4(1+k_2^2)}}{1+k_2^2} \tag{6}$$

In which (5) and (6):

$$k_1=\frac{k_5-2l_{01}l_{11}\cos\theta_{11}+2l_{02}l_{12}\cos\theta_{12}}{2l_{11}\sin\theta_{11}-2l_{12}\sin\theta_{12}} \tag{7}$$

$$k_2=\frac{l_{11}\cos\theta_{11}+l_{12}\cos\theta_{12}-l_{01}-l_{02}}{l_{11}\sin\theta_{11}-l_{12}\sin\theta_{12}} \tag{8}$$

$$k_3=k_1k_2-k_2l_{11}\sin\theta_{11}+l_{11}\cos\theta_{11}-l_{01} \tag{9}$$

$$k_4=l_{11}^2+k_1^2+l_{01}^2-l_{14}^2-2k_1l_{11}\sin\theta_{11}-2l_{01}l_{11}\cos\theta_{11} \tag{10}$$

In which (7):

$$k_5=l_{11}^2-l_{12}^2+l_{01}^2-l_{02}^2+l_{13}^2-l_{14}^2 \tag{11}$$

Above all, the forward kinematics solution of the driving unit is completed.

B. *Kinematic Analysis of Follower Unit*

The geometric relations of links in the follower unit n are shown in Fig. 7. The lengths of $A_{n1}B_{n2}$ and $A_{n3}B_{n2}$ are $l_{(n-1)3}$ and $l_{(n-1)4}$, the lengths of $A_{n1}C_{n3}$ and $A_{n3}C_{n1}$ are l_{n1} and l_{n2}. The lengths of passive links $C_{n1}D_{n2}$, $C_{n3}D_{n2}$ and $B_{n2}D_{n2}$ are l_{n3}, l_{n4} and l_{n5}, respectively. The angles between l_{n1}, l_{n2} and fixed rib plate $B_{n1}B_{n2}B_{n3}$ respectively are θ_{n1} and θ_{n2}. The angles between l_{n3}, l_{n4} and dynamic rib plate $D_{n1}D_{n2}D_{n3}$ respectively are θ_{n3} and θ_{n4}. The angles between l_{n5} and current coordinate system x axis are θ_{n5}.

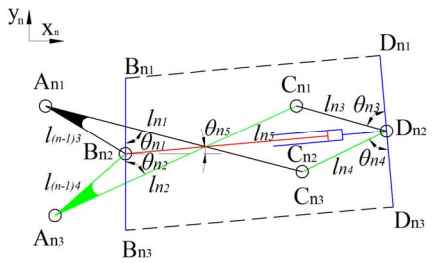

Fig. 7 Kinematic model of follower unit n.

The origin of the follower unit n coordinate system is B_{n2}, the X axis is along the direction of $B_{n2}D_{n2}$, and the Y axis is along the direction of $B_{n2}B_{n1}$. Position of the moving-ribbed plate in follower unit n can be described by two coordinates:

$$\mathbf{q_n}=[x_{Dn2},y_{Dn2}]^{\mathrm{T}} \tag{12}$$

Where x_{Dn2} and y_{Dn2} are the positions of the moving-ribbed plate in the follower unit n coordinate system, θ_{n5} is the angle between the fixed-ribbed plate and the moving-ribbed plate in the follower unit n. For the follower unit n, there exist the following constraint equations:

$$\mathbf{\Phi(q_n)}=\begin{bmatrix} l_{n1}\sin\theta_{n1}-l_{(n-1)3}\sin\theta_{(n-1)3}+l_{n4}\sin(\theta_{n4}-\theta_{n5})-x_{Dn2} \\ l_{n2}\sin\theta_{n2}-l_{(n-1)4}\sin\theta_{(n-1)4}+l_{n3}\sin(\theta_{n3}+\theta_{n5})-x_{Dn2} \\ l_{n5}\cos\theta_{n5}-x_{Dn2} \\ -l_{n1}\cos\theta_{n1}+l_{(n-1)3}\cos\theta_{(n-1)3}+l_{n4}\cos(\theta_{n4}-\theta_{n5})-y_{Dn2} \\ l_{n2}\cos\theta_{n2}-l_{(n-1)4}\cos\theta_{(n-1)4}-l_{n3}\cos(\theta_{n3}+\theta_{n5})-y_{Dn2} \\ l_{n5}\sin\theta_{n5}-y_{Dn2} \end{bmatrix} \tag{13}$$

From (13), there is:

$$l_{n4}^2=(-f_{n1}\sin\theta_{n1}+x_{Dn2})^2+w_{n4}^2 \tag{14}$$

$$l_{n3}^2=(-f_{n2}\sin\theta_{n2}+x_{Dn2})^2+w_{n3}^2 \tag{15}$$

In which (14) and (15):

$$f_{n1}=l_{n1}-l_{(n-1)3}\frac{\sin\theta_{(n-1)3}}{\sin\theta_{n1}} \tag{16}$$

$$f_{n2}=l_{n2}-l_{(n-1)4}\frac{\sin\theta_{(n-1)4}}{\sin\theta_{n2}} \tag{17}$$

$$w_{n3}=f_{n2}\cos\theta_{n2}-l_{(n-1)4}\cos\theta_{(n-1)4}-y_{Dn2} \tag{18}$$

$$w_{n4}=f_{n1}\cos\theta_{n1}-l_{(n-1)3}\cos\theta_{(n-1)3}+y_{Dn2} \tag{19}$$

In the kinematic analysis, the inputs and outputs are concerned (14) and (15) can be rewritten as:

$$x_{Dn2}=k_{n1}+\frac{-k_{n2}k_{n3}+k_{n2}\sqrt{k_{n3}^2-k_{n4}(1+k_{n2}^2)}}{1+k_{n2}^2} \tag{20}$$

$$y_{Dn2}=\frac{-k_{n3}+\sqrt{k_{n3}^2-k_{n4}(1+k_{n2}^2)}}{1+k_{n2}^2} \tag{21}$$

In which (20) and (21):

$$k_{n1}=\frac{k_{n5}-2f_{n1}f_{n3}\cos\theta_{n1}+2f_{n2}f_{n4}\cos\theta_{n2}}{2f_{n1}\sin\theta_{n1}-2f_{n2}\sin\theta_{n2}} \tag{22}$$

$$k_{n2}=\frac{f_{n1}\cos\theta_{n1}+f_{n2}\cos\theta_{n2}-f_{n3}-f_{n4}}{f_{n1}\sin\theta_{n1}-f_{n2}\sin\theta_{n2}} \tag{23}$$

$$k_{n3}=k_{n1}k_{n2}-k_{n2}f_{n1}\sin\theta_{n1}+f_{n1}\cos\theta_{n1}-f_{n3} \tag{24}$$

$$k_{n4}=f_{n1}^2+k_{n1}^2+f_{n3}^2-l_{n4}^2-2k_{n1}f_{n1}\sin\theta_{n1}-2f_{n1}f_{n3}\cos\theta_{n1} \tag{25}$$

In which (22), (23), (24) and (25):

$$k_{n5}=f_{n1}^2-f_{n2}^2+f_{n3}^2-f_{n4}^2+l_{n3}^2-l_{n4}^2 \tag{26}$$

$$f_{n3}=l_{(n-1)3}\cos\theta_{(n-1)3} \tag{27}$$

$$f_{n4}=l_{(n-1)4}\cos\theta_{(n-1)4} \tag{28}$$

Above all, the forward kinematics solution of the follower unit is completed.

C. *Kinematic Analysis of Morphing Wing*

In this work, the Rapture 40 UAV was designed as a reference model, and the wingspan of the morphing wing is 1200mm. The morphing wing is composed of one driving unit and two follower units in series, and adopts modular design.

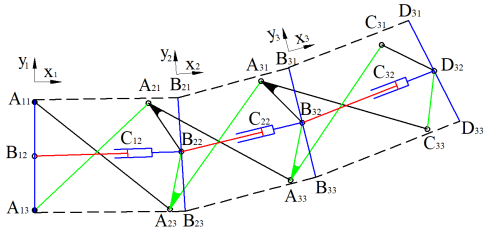

Fig. 8 Kinematic model of morphing skeleton.

The geometrical relationships of the three units are shown as Fig. 8. In the morphing wing model, the morphing skeleton is modularized to reduce the types of members. The parameters are selected as follows: $l_{11}=l_{12}=l_{21}=l_{22}=l_{31}=l_{32}$,

$l_{13}=l_{14}=l_{23}=l_{24}=l_{33}=l_{34}$, $l_{01}=l_{02}=50\text{mm}$. l_5 is the length of the horizontal projection of the wingspan. θ_5 is the bending angle of the tip of morphing wing. Apparently, there is a relationship:

$$l_5 = l_{15}\cos\theta_{15} + l_{25}\cos\theta_{25} + l_{35}\cos\theta_{35} \tag{29}$$

$$\theta_5 = \theta_{15} + \theta_{25} + \theta_{35} \tag{30}$$

For the morphing wing, there are the following constraint equations:

$$\begin{cases} \mathbf{\Phi}(\mathbf{q}_1) = \mathbf{0} \\ \mathbf{\Phi}(\mathbf{q}_2) = \mathbf{0} \\ \mathbf{\Phi}(\mathbf{q}_3) = \mathbf{0} \end{cases} \tag{31}$$

From (31), we obtain in the global coordinate system:

$$x_D = x_{D12} + x_{D22} + x_{D32} \tag{32}$$

$$y_D = y_{D12} + y_{D22} + y_{D32} \tag{33}$$

Where x_D and y_D are the positions of the morphing wing in the global coordinate system. Above all, the forward kinematics solution of the morphing wing is completed.

IV. Comparative Analysis of the Morphing Wing

A. Initial State of Morphing Wing

The initial state of morphing wing units is horizontal contraction. In this state, the wingspan is in the minimum length 1200mm and the bending angle is 0 degrees.

$$l_{50} = \sqrt{l_{13}^2 - l_{01}^2} + 3\sqrt{l_{11}^2 - (l_{01}+l_{02})^2} = 1200\text{mm} \tag{34}$$

$$\theta_{150} = \theta_{250} = \theta_{350} = 0° \tag{35}$$

In which (34) and (35), l_{50} is the length of the horizontal projection of the wingspan in the initial state of morphing wing, the angles between l_{n5} and coordinate system of unit x axis in the initial state of morphing wing are θ_{n50}.

B. Boundary Condition

The geometric parameters of the morphing wing units need to satisfy the following constraints and inequalities to avoid intersections of the links:

$$-l_{01} \le l_{n3}\cos\theta_{n3} \le l_{01} \tag{36}$$

$$-l_{01} \le l_{n4}\cos\theta_{n4} \le l_{01} \tag{37}$$

The geometry of the morphing wing units is defined by nondimensional parameters k (link length ratio $k = l_{11}/l_{13}$). According to the different k-values, the follower unit of morphing wing are divided into the following five types. As shown in Fig. 9, named as (a) $k = k_{\max}$, (b) $k_{\max} > k > 2$, (c) $k = 2$, (d) $2 > k > k_{\min}$, (e) $k = k_{\min}$. The related parameters are selected as follows: $k_{\max}$=4.12, $k_{\min}$=1.04.

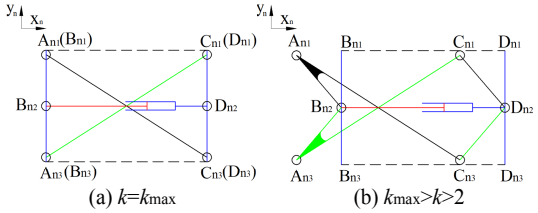

(a) k=$k$max (b) $k$max>k>2

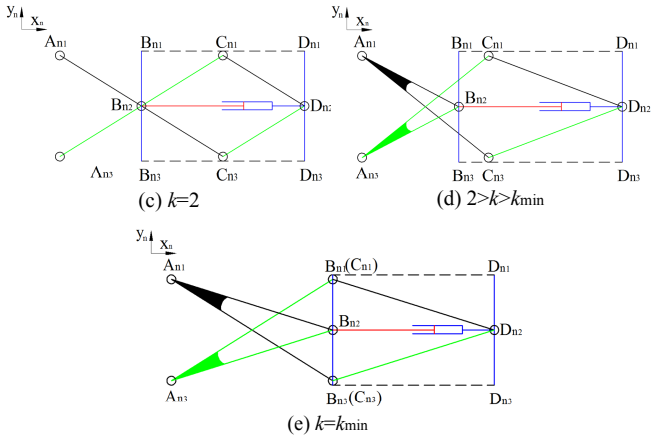

(c) k=2 (d) 2>k>$k$min

(e) k=$k$min

Fig. 9 Five different k-values of the morphing unit.

C. Kinematical comparisons with different k-values

In order to analyze the kinematics of the morphing wing with different k-values, monitor the motions of the virtual prototype mechanism using commercial software ADAMS according to the selected mechanism parameters.

When the wing-span is extended, the rotational speed w_{11} of the driving joint A_{11} is 0.017rad/s, and the driving direction is counterclockwise; the rotational speed w_{13} of the driving joint A_{13} is 0.017rad/s, and the driving direction is clockwise.

when $k = k_{\max}$, it is found that the morphing wing is in self-locking state and cannot be extended and bent according to ADAMS simulation model. According to the different k-values, the maximum extension of morphing wing is divided into the following four types. As shown in Fig. 10, named as (a), (b), (c), (d). The related parameters are selected as follows: k = 3.52, k = 2, k = 1.37, k = 1.04.

In global coordinate system, once the three-point y-direction coordinates of A_{23}, A_{33}, and C_{33} are greater than 50mm or less than -50mm, the wing skeleton will interfere with the skin. Now the paper will measure the y-direction coordinates of A_{23}, A_{33} and C_{33} and the x-direction coordinates of B_{23}, A_{33} and C_{33} as a function of time. The maximum extension of different k morphing wing is shown in Fig. 10.

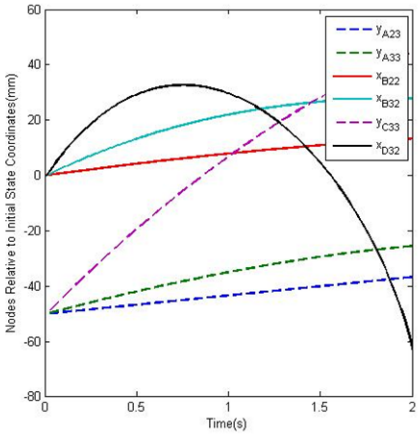

(a) k=3.52($k$max>k>2)

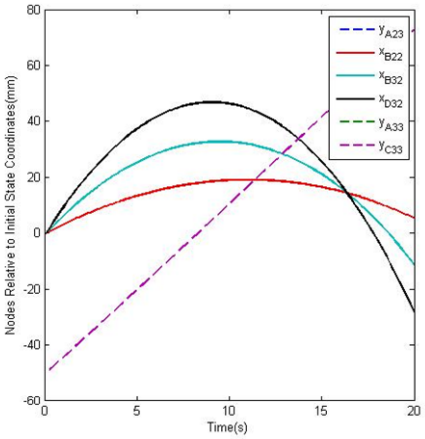

(b) k=2

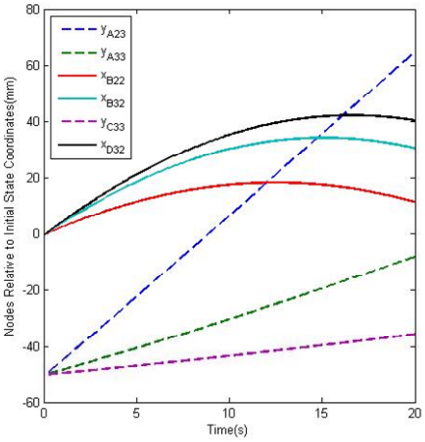

(c) k=1.37(2>k>$kmin$)

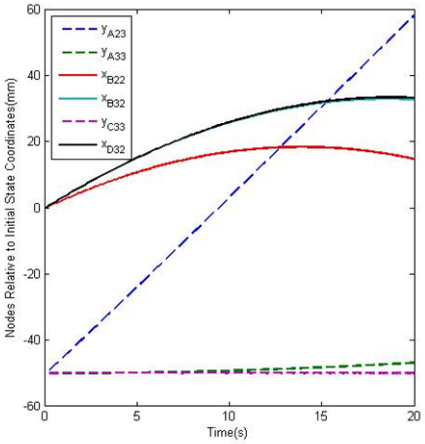

(d) k=1.04(k=$kmin$)

Fig. 10 The extension of different k-valued morphing wing.

As shown in Fig. 10, when k=3.52, 2, 1.37, 1.04 the extension of morphing wing reaches its maximum at 0.85s, 8.93s, 16.5s, 18.4s and the maximum extension is 31.92mm, 46.81mm, 42.22mm, 33.34mm.

As shown in Fig. 10, the morphing wing achieves the maximum extension at k=2. When k_{max}>k>2, the maximum extension of morphing wing increases with the increase of k-value; when 2>k>$\underline{k}_{min}$, he maximum extension of morphing wing decreases with the increase of k-value.

D. Kinematical comparisons with different m-values

In this paper, the upside and downward bending morphing wing is symmetrical, so the upside bending morphing wing is analyzed at the same time k is 2. According to kinematics analysis, the morphing wing can achieve different maximum bending angles with different m-values(m=w_{11}/w_{13}).

The rotational speed w_{11} of the driving joint A_{11} is 0.034rad/s, and the driving direction is counterclockwise; the driving direction of the driving joint A_{13} is clockwise. In order to achieve the upward bending of wing span, m needs to be greater than 1. The morphing wing can analyze the following four bending conditions according to the driving speed ratio m. As shown in Fig. 11, named as (a), (b), (c), (d). The related parameters are selected as follows: m=1.1, m=2, m=4, m=8.

As shown in Fig. 11, when m=1.1, 2, 4, 8 the bending angle of morphing wing reaches its maximum at 4.24s, 4.90s, 5.31s, 5.46s and the maximum bending angle is 17.6°, 17.5°, 17.4°, 17.1°.

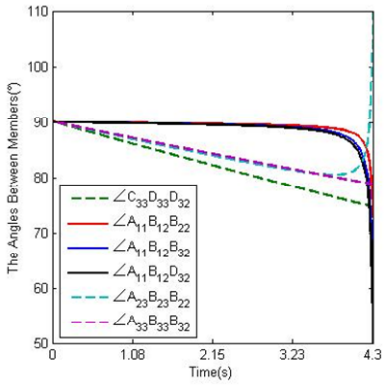

(a) m=1.1

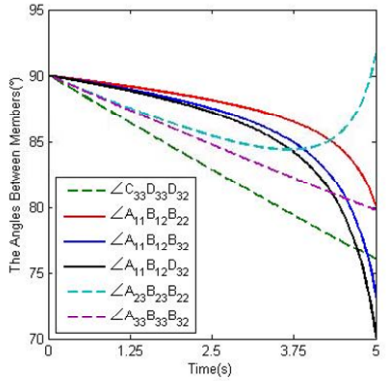

(b) m=2

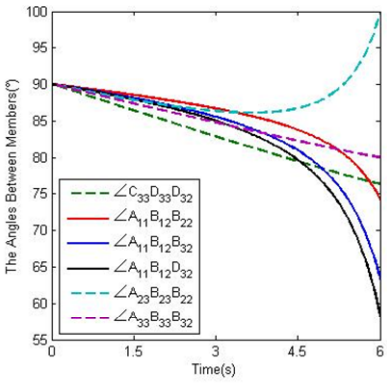

(c) m=4

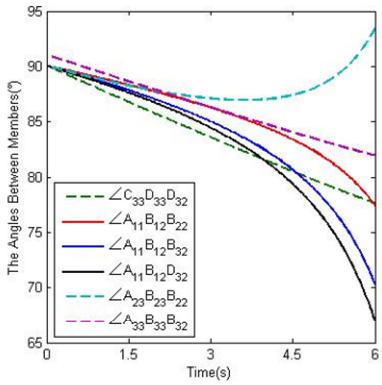

(d) m=8

Fig. 11 The bending angle of different m-valued morphing wing.

In global coordinate system, once the position angle $\angle A_{23}B_{23}B_{22}$, $\angle A_{33}B_{33}B_{32}$, $\angle C_{33}D_{33}D_{32}$are greater than 90°, the wing skeleton will interfere with the skin. Now the paper will measure the position angle $\angle A_{23}B_{23}B_{22}$, $\angle A_{33}B_{33}B_{32}$, $\angle C_{33}D_{33}D_{32}$ and the position angle $\angle A_{11}B_{12}B_{22}$, $\angle A_{11}B_{12}B_{32}$, $\angle A_{11}B_{12}D_{32}$ as a function of time. The maximum bending angle of different m-valued are shown in Fig. 11.

As shown in Fig. 11, the morphing wing achieves the maximum bending angle at m=1.1 compared with other m-values. The maximum bending angle of morphing wing decreases with the increase of m-values.

V. Conclusions

In this paper, a new variable-span and cambered span morphing wing for UAV is designed to improve the aerodynamic performance. The morphing skeleton of wing is composed of the unit which is seven-bar mechanism in series. The rubber-filled corrugated sandwich corrugated skin is designed to satisfy the deformation. The kinematic equations are established according to the design of the morphing wing structure. The relationship between deformation law and driving angle is obtained. At the same time, influence law of various k-values and m-values for the morphing wing on were also analyzed.

As the results of simulation shown, that the different k-values has a great influence on the maximum extension of morphing wings. When the k-value is fixed, the different m-values has a great influence on the maximum bending angle of the morphing wing. When link length ratio k is 2, the morphing wing achieves the maximum extension. Especially when k is 2 and driving speed ratio m is 1.1, the morphing wing achieves the maximum bending angle. This will be helpful for application of the morphing wing and more work will to be done in the future.

References

[1] S. Barbarino, M. Friswell, D. Inman, et al, "A Review of Morphing Aircraft," Journal of Intelligent Material Systems and Structures, vol. 22, no. 9, pp. 823-877, June 2011.

[2] J. Valasek, Morphing Aerospace Vehicle and Structure, New York, CA: Hoboken, 2012.

[3] C. Thill, J. Etches, I. Bond, et al, "Morphing skins," The Aeronautical Journal, vol.112, no. 1129, pp. 117-139, March 2008.

[4] S. Kota, et al, "Design and application of compliant mechanisms for morphing aircraft structures," Smart Structures and Materials, vol. 5054, no. 2, pp. 24-33, August 2003.

[5] R. Ajaj, C. Beaverstock, M. Friswell, "Morphing aircraft: The need for a new design philosophy," Aerospace Science and Technology, vol. 49, pp. 154-166, February 2016.

[6] D. Li, S. Zhao, A. Ronch, et al, "A review of modelling and analysis of morphing wings," Progress in Aerospace Sciences, vol. 100, pp. 46-62, June 2018.

[7] S. Hao, T. Ma, W. Gan, et al. "Static aeroelastic characteristics analysis of high-aspect-ratio wing for hydrogen-powered UAV," Journal of Beijing University of Aeronautics & Astronautics, vol. 43, no. 8, pp. 1670-1676, 2017.

[8] B. Gao, "Deployable Mechanism Design for Span Morphing Wing Aircraft," Tianjin: Master's degree thesis of Tianjin University, 2016.

[9] V. Sherrer, T. Hertz and M. Shirk, "Wind Tunnel Demonstration of Aeroelastic Tailoring Applied to Forward Swept Wings," Journal of Aircraft, vol. 18, no. 11, pp. 976-983, 2015.

[10] S. Lucato, J. Wang, P. Maxwell, et al, "Design and demonstration of a high authority shape morphing structure," International Journal of Solids and Structures, vol. 41, no. 13, pp. 3521–3543, June 2004.

[11] E. Abrahamson, M. Lake, N. Munshi, et al, "Shape memory mechanics of an elastic memory composite resin," Journal of Intelligent Material Systems and Structures, vol. 14, no. 10, pp. 623-632, October 2003.

[12] C. Thill, J. Etaches, I, Bond, et al, "Composite corrugated structures for morphing wing skin applications," Smart Materials and Structures, vol. 19, no. 12, pp. 1-11, November 2010.

[13] T. Yokozeki, S. Takeda, T. Ogasawara, et al, "Mechanical properties of corrugated composites for candidate materials of flexible wing structures," Composites Part A: Applied Science and Manufacturing, vol. 37, no. 10, pp. 1578-1586, October 2006.

[14] K. Olympio, F. Gandhi, "Flexible skins for morphing aircraft using cellular honeycomb cores," Journal of Intelligent Material Systems and Structures, vol. 21, no. 17, pp. 1719-1735, 2010.